Journal of Inorganic and General Chemistry
ZAAC
Zeitschrift für anorganische und allgemeine Chemie

DOI: 10.1002/zaac.202100043

ARTICLE

Temperature dependent crystal structure re-determination and electronic properties of UI_3

Malte Sachs,[a] Lars Deubner,[a] Martin Möbs,[a] Markus Hoelzel,[b] Matthias Conrad,[a] and Florian Kraus*[a]

Dedicated to Prof. Dr. Josef Breu on the Occasion of his 60th Birthday

In this work, we have re-investigated the structural and physical properties of UI_3 by means of temperature dependent powder neutron diffraction, heat capacity and magnetic measurements. We confirm that UI_3 crystallizes in the $PuBr_3$ structure type, space group *Cmcm*. We did not observe any temperature dependent structural phase transition in the temperature range from 10 to 300 K. We further report the first quantum chemical calculations of UI_3 by density functional theory (DFT). The calculated structural and electronic properties demonstrate the pronounced two-dimensional anisotropic effects present in UI_3 due to its layered structure.

1. Introduction

Uranium(III) iodide belongs to the group of layered lanthanoid and actinoid halides that crystalize in the $PuBr_3$ (*Cmcm*, *oS*16) structure type. Since the first determination of its crystal structure in 1948 by Zachariasen[1] several further studies were performed investigating its structural,[2–4] magnetic[3,5,6] and thermodynamic properties.[5] Below 3.2 K it undergoes an antiferromagnetic transition forming a magnetic $2\times2\times2$ superstructure compared to the paramagnetic unit cell.[3] That far, no single crystal structure determination of UI_3 had been performed. This is probably due to the fragile needle-shaped crystals which UI_3 forms and the layers within the crystal structure, that easily disorder upon handling the compound.

We recently reported a new synthesis route for pure, solvent-free and single-crystalline UI_3 and other uranium(III) halides making the determination of its single crystal structure possible.[4] The assignment to the $PuBr_3$ structure type with the space group *Cmcm* of previous investigations could be confirmed. However, our diffraction data at 100 K revealed several weak reflections violating the extinction condition of the *c*-glide plane. A $\lambda/2$ contribution as source for these reflections could be ruled out, as well as a lower symmetric space group containing no *c*-glide plane. This raised the question if a phase transition between room temperature and 100 K would take place leading to the observed diffraction pattern. We present here the re-investigation of the structural and physical properties of UI_3 by means of temperature dependent powder neutron diffraction, heat capacity as well as magnetic measurements. To the best of our knowledge, no quantum chemical calculations of UI_3 were reported so far. We thus calculated the structural and electronic properties of UI_3 by density functional theory (DFT) with a focus on its layer structure and the consequences thereof.

2. Results and Discussion

2.1. Powder neutron diffraction on UI_3

To investigate a possible phase transition of UI_3 we have performed powder neutron diffraction on polycrystalline UI_3 at temperatures of 298, 100, and 10 K. Figure 1 displays the diffraction pattern and the Rietveld refinement of UI_3 obtained at 10 K. The diffraction patterns recorded at 100 and 298 K, as well as the technical details of the refinements are given in the Supporting Information.

All three data sets could be refined successfully using the structural model of the $PuBr_3$ structure type (*Cmcm*, *oS*16). Small additional reflections are present in the diffractograms. They can be indexed with the lattice parameters of Si ($Fd\bar{3}m$, *cF*8). Silicon was used in our synthesis of UI_3 working as reducing agent of UI_4 ($4\ UI_4 + Si \rightarrow 4\ UI_3 + SiI_4$), details are reported elsewhere.[4]

The Rietveld refinement reveals an amount of less than one wt% silicon in our samples.

In the powder neutron diffraction patterns no reflections violating the extinction condition of the *c*-glide plane were observed as in the single crystal data.

[a] M. Sachs, L. Deubner, M. Möbs, M. Conrad, F. Kraus
Fachbereich Chemie, Philipps-Universität Marburg, Hans-Meerwein-Straße 4,
35032 Marburg, Germany
E-mail: florian.kraus@chemie.uni-marburg.de
[b] M. Hoelzel
Heinz Maier-Leibnitz Zentrum (MLZ), Technische Universität München, Lichtenbergstr. 1, 85747 Garching, Germany

Supporting information for this article is available on the WWW under https://doi.org/10.1002/zaac.202100043

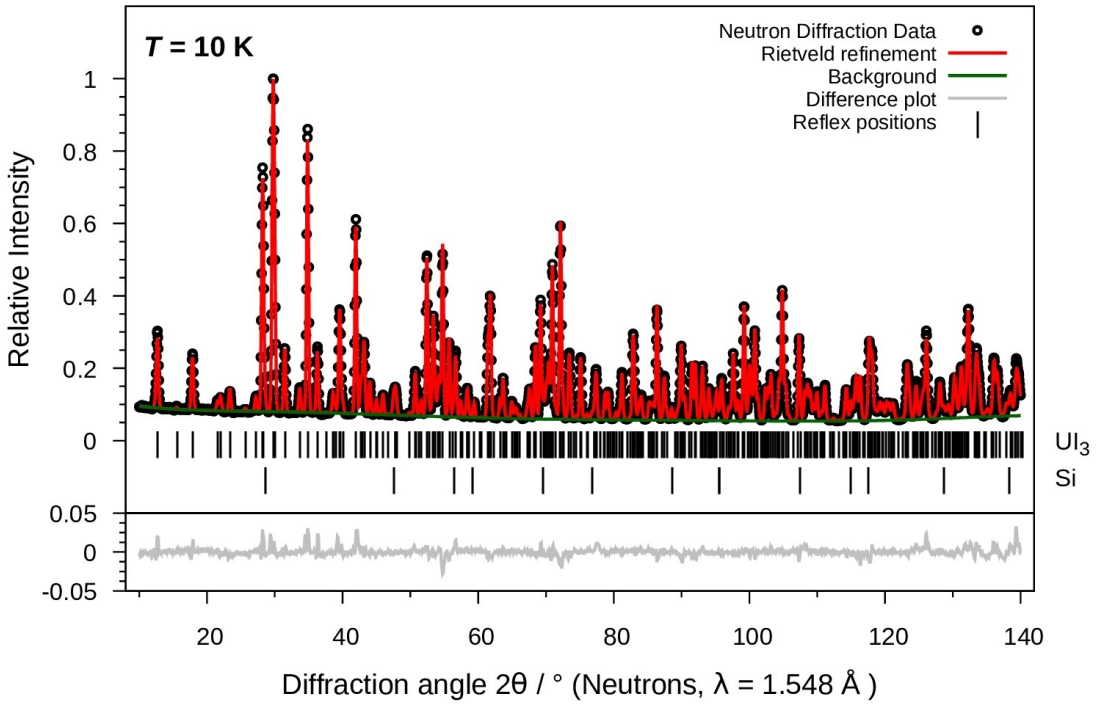

Figure 1. Powder neutron diffraction pattern (wavelength $\lambda = 1.548$ Å) and Rietveld refinement of UI_3 at 10 K: measured data points (circles), calculated diffractogram (red), background (green) and difference curve (grey). Vertical bars indicate the calculated reflection positions of UI_3 (upper trace) and Si (lower trace). The amount of Si is determined to be less than 1 wt%. Profile *R* factors (corrected for background): $R_p^* = 5.1\,\%$, $wR_p^* = 5.6\,\%$, GOF = 3.54.

All reflections could be unambiguously indexed within the $PuBr_3$ structural model. Table 1 and Table 2 contain the lattice parameters and the structural parameters of UI_3 compared to literature values, respectively.

Overall, our results agree with the reported neutron diffraction data of Murasik and coworkers with the exception that we determined the lattice parameters more accurately.[3] We find a pronounced anisotropy in the temperature dependent contraction of the lattice parameters. The shrinkage of the lattice parameter *a* between 298 and 10 K is with 0.02 Å three to five times smaller than the shrinkage in the *b* and *c* direction,

Table 1. Refined lattice parameters of UI_3 in comparison to literature data.

Temperature *T*/K	Measurement type	*a*/Å	*b*/Å	*c*/Å	Reference
298	Neutrons/powder	4.33625(6)	14.0063(3)	10.0055(2)	This work
	Neutrons/powder	4.328(5)	14.01(2)	10.01(1)	[2]
	Neutrons/powder	4.334(6)	14.02(2)	10.01(2)	[3]
	X-rays/powder	4.3339(2)	13.9996(5)	9.9992(3)	[4]
100	Neutrons/powder	4.32400(4)	13.9415(2)	9.9457(1)	This work
	X-rays/single crystal	4.3208(9)	13.923(3)	9.923(2)	[4]
10	Neutrons/powder	4.32028(4)	13.9209(2	9.9319(1)	This work
4.2	Neutrons/powder	4.324(6)	13.93(2)	9.94(2)	[3]

Table 2. Temperature dependency of structural parameters of UI_3 compared to literature data. All data are from powder neutron diffraction.

T/K	*y*(U)	*y*(I1)	*y*(I2)	*z*(I2)	B_{iso}(U)/Å^2	B_{iso}(I1)/Å^2	B_{iso}(I2)/Å^2	Reference
298	0.74276(7)	0.0791(2)	0.35482(8)	0.06506(7)	1.11(3)	1.51(2)	1.37(2)	This work
	0.7439(6)	0.0812(7)	0.3571(5)	0.0646(5)	1.8(1)	1.4(1)	1.4(1)	[3]
100	0.74222(5)	0.07839(9)	0.35546(6)	0.06482(5)	0.49(2)	0.59(2)	0.54(2)	This work
10	0.74231(5)	0.07803(8)	0.35572(6)	0.06464(5)	0.28(2)	0.23 (2)	0.27(2)	This work
4.2	0.7426(6)	0.0744(7)	0.3563(6)	0.0645(6)	1.1(2)	−0.5(1)	−0.5	[3]

respectively. We note that the *a* axis is also the magnetic easy axis of the low-temperature antiferromagnetic phase.[3]

The structural parameters given in Table 2 essentially agree with the literature.[3] However, we obtain much more precise displacement parameters with a physically sound negative temperature dependency. Performing a linear regression of the obtained displacement parameters, we can extrapolate them to a value of around 0.2 Å^2 at 0 K.

In summary, neutron powder diffraction gave no hint for a phase transition and we proceed discussing the results of the temperature dependence of selected physical properties of UI_3.

2.2. Heat capacity and magnetic measurements

We performed heat capacity and magnetic measurements of UI_3 between 100 and 300 K to receive hints of a possible phase transition in this temperature range. Literature data only give a rough step size in this temperature range so that effects of a phase transition could have been overlooked.[5,6] Figure 2a displays the results of the heat capacity measurements between 1.8 and 300 K.

Due to the way the sample is prepared (see Section 4.3) the data should only be interpreted qualitatively. Second order phase transitions should yield peaks in the heat capacity data resulting from the change in entropy during the phase transition. As shown in Figure 2a, the heat capacity proceeds smoothly between 300 and 100 K giving no evidence for a phase transition in this temperature range. The inset of Figure 2a displays the heat capacity effect of the antiferromagnetic transition at 3.2 K that is in good agreement with previous measurements thus proving the sample purity.

Figure 2b displays the inverse magnetic susceptibility of UI_3 between 300 and 1.8 K. The antiferromagnetic transition at about 3 K is again clearly visible. There is no evidence of a phase transition in the smoothly varying magnetic susceptibility data between 100 and 300 K, and hence again there is no evidence for a structural change that could cause the observed single crystal X-ray diffraction pattern with the violations of the extinctions due to the *c*-glide plane. The data can be fitted with a modified Curie-Weiß law: $\chi = C/(T-\theta)+\chi_0$ between 50 and 300 K. The fit parameters are: $C = 1.765(2)$ K cm^3 mol^{-1} (3.76 μ_B), $\theta = -83.3(2)$ K and $\chi_0 = 603(4)\ 10^{-6}$ cm^3 mol^{-1}. The effective magnetic moment of 3.76 μ_B is in good agreement with those reported for other uranium(III) halides (UCl_3: 3.70 μ_B, UBr_3: 3.57 μ_B, UI_3: 3.65 μ_B)[6] and is close to the theoretical free-ion value of 3.69 μ_B calculated for the $^4I_{9/2}$ ground state with intermediate coupling.[6]

Neither the heat capacity and magnetic measurements, nor the neutron powder diffraction experiments gave any hint for a phase transition to a structure without a *c*-glide plane that could explain the observed single crystal diffraction pattern.[4] We checked the reciprocal space for a possible twin with a very small twin fraction in our single crystal structure determination that would give rise to the observed weak reflections violating the extinction condition. Another reason for the discrepancy between powder neutron diffraction and single crystal X-ray diffraction data may be due to a superstructure or a disordered packing of the individual layers within the UI_3 crystal. As the *c*-glide plane operator connects uranium atoms of different UI_3 layers by symmetry, superstructures along the *b* axis as the packing direction could result in the observed violation of the extinction condition. Packing variants related to polytypism occur frequently in van der Waals packed layer structures.[7–9] However, we do not favor this explanation as we have no evidence in that direction. What we now deem likely is that the weak reflections that violated the extinction condition for the *c*-glide plane were due to the Renninger-effect.[10] For the groups

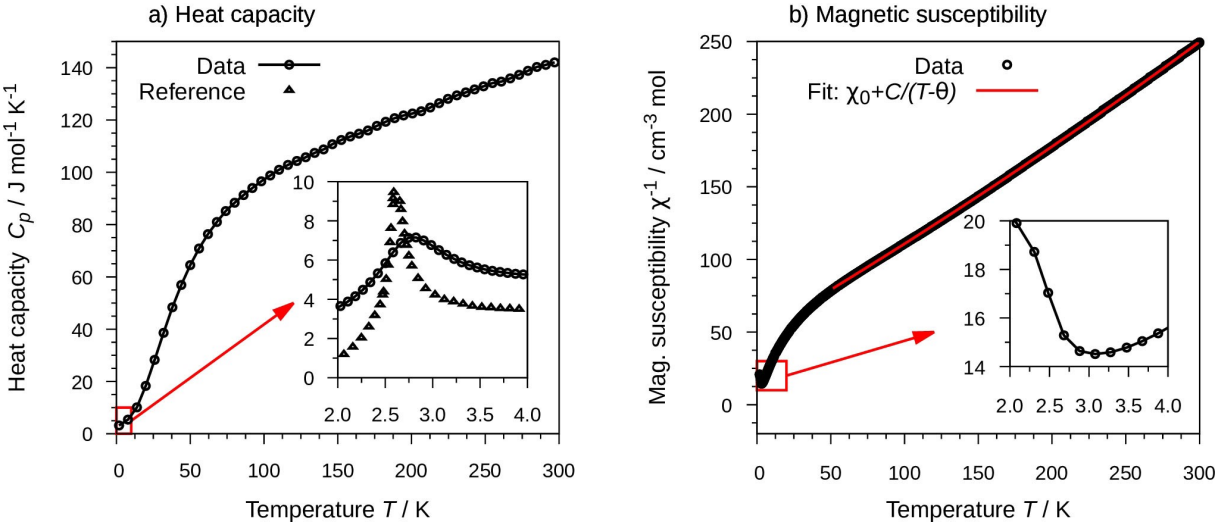

Figure 2. Temperature dependent physical properties of UI_3 between 1.8 and 300 K. a) The isobaric heat capacity C_p (circles). The inset displays the effect of the antiferromagnetic transition at 3.2 K in comparison to previous measurements (triangles).[5] b) The inverse molar magnetic susceptibility χ^{-1} at a field of 10 kOe (circles) and fit (red) by a modified Curie-Weiß law ($\chi = C/(T-\theta)+\chi_0$) with the fitting constants $C = 1.765(2)$ K cm^3 mol^{-1}, $\theta = -83.3(2)$ K, $\chi_0 = 603(4)\ 10^{-6}$ cm^3 mol^{-1}). The inset displays the antiferromagnetic transition at 3.2 K.

of symmetry-equivalent reflections that violate the extinction condition there is one or sometimes two with distinctly stronger intensity compared to the others.

With this, we want to end the discussion of the experimental results and continue presenting our theoretical investigations on UI_3 by means of DFT.

2.3. Quantum chemical calculations

The layered structure of uranium(III) iodide should induce a two-dimensional anisotropy in its physical properties: strong bonding interactions within the layers and weaker van der Waals forces between them. We have performed quantum chemical calculations using DFT on UI_3 to demonstrate this effect. The computational details are given in Section 4.4.

The occurrence of van der Waals forces between the UI_3 layers perpendicular to the *b* axis can simply be demonstrated by performing structural optimizations including and excluding dispersion interactions. We have performed such calculations and present their results in Table 3. As the plain PBE functional does not include dispersion interactions, the lattice parameter *b* perpendicular to the van der Waals packed layers drastically increases during the structural optimization. A lattice parameter *b* of 15.7246 Å is obtained that way that is by more than 1.8 Å larger than the observed lattice parameter *b* of 13.9209(2) Å. However, the *a* and *c* lattice parameters agree with the experiment. Including the semi-empirical D3 dispersion interactions of Grimme and coworkers,[11,12] the optimized lattice parameter *b* of 14.0141 Å is in better agreement to the experimentally determined value. This demonstrates the impact of the van der Waals forces between the UI_3 layers.

The dispersion corrections can improve the accurateness of the prediction of the lattice parameter *b* of UI_3. However, it worsens the agreement to experiment of the *a* and *c* lattice parameters compared to the plain PBE calculations as given in Table 3. The prediction of the structural properties of UI_3 can be improved further by performing DFT + *U* calculations as a second correction for the PBE functional. DFT + *U* can improve the description of strong onside Coulomb correlation effects of the electrons in the uranium *f* orbitals that are underestimated in plain LDA and GGA calculations.[13,14] We have calculated the Hubbard-*U* parameter of UI_3 *ab initio* by Density-Functional-Perturbation Theory (DFPT).[15] Details are given in Section 4.4. However, we note that the so derived Hubbard-*U* parameter of 2.6 eV is strongly dependent on the chosen basis set and the projection type of the Hubbard-calculation.[13,15] Using the Hubbard-*U* correction together with the D3 dispersion corrections denoted as PBE + D3 + *U* yield satisfactory results for the structural optimization of UI_3 with lattice parameters not differing more than 0.5 % compared to observed ones.

Figure 3a) displays the crystal structure of UI_3. The picture highlights the bicapped trigonal prismatic coordination sphere of the uranium atoms and the van der Waals gaps between the individual $^{2}_{\infty}[UI_{\frac{2}{2}}I_{\frac{6}{3}}]$ layers packed along the *b* axis.

To demonstrate the different bonding interactions within and between the UI_3 layers, we have calculated electron density difference maps. They display the difference of the electron density of the compound compared to a superposition of the electron density of free atoms and show where electron density is increased or decreased. Figure 3b contains a section of an electron density difference map parallel to the $(0\bar{2}3)$ plane and including the point 0, $^1/_2$, $^1/_2$. It contains two UI_3 layers. Within the layers, the electron density adopts large absolute values. This demonstrates that the electron density of the free ions is strongly modified during the self-consistent field procedure accounting for the strong bonding interactions within the layers. In contrast, the electron density in the van-der Waals gaps nearly stays unchanged illustrating the weak interactions between the layers. Only a small fraction of difference electron density of the iodine atoms is pointing towards this gap, which could be interpreted as lone pairs of the iodide anions. The electron density around the iodine atoms increases compared to the density of the free atoms. This is in line with their oxidation state of –I. Moreover, their electron density is strongly polarized towards the U atoms within the layer. The electron density of the uranium atoms decreases as is expected from its positive oxidation state of +III in the compound UI_3. However, the density decrease occurs next to the U–I bonds. A part of the electron density of the uranium atoms is increased at this contact line hinting to covalent bonding interactions alongside the expected ionic interactions between these atoms. The difference electron difference map thus highlights the strong

Table 3. DFT results of the structure optimization of UI_3 at 0 K compared to our experimentally obtained data at 10 K. Three different optimization methods are used: PBE, PBE + D3 and PBE + D3 + *U* (sr-PAW/PBE + spin polarization, *U* = 2.60 eV). Details are given in Section 4.4.

Lattice parameters / Å	PBE	PBE + D3	PBE + D3 + *U*	Experiment at 10 K
a	4.2328	4.1408	4.3418	4.32028(4)
b	15.7246	14.0141	13.8779	13.92087(18)
c	9.9945	9.8466	9.9093	9.93197(11)
Variable Atomic coordinates				
y (U)	0.7383	0.739	0.7416	0.74231(5)
y (I1)	0.0921	0.0748	0.0759	0.07803(8)
y (I2)	0.3439	0.3560	0.3559	0.35572(6)
z (I2)	0.0673	0.0647	0.0642	0.06464(5)

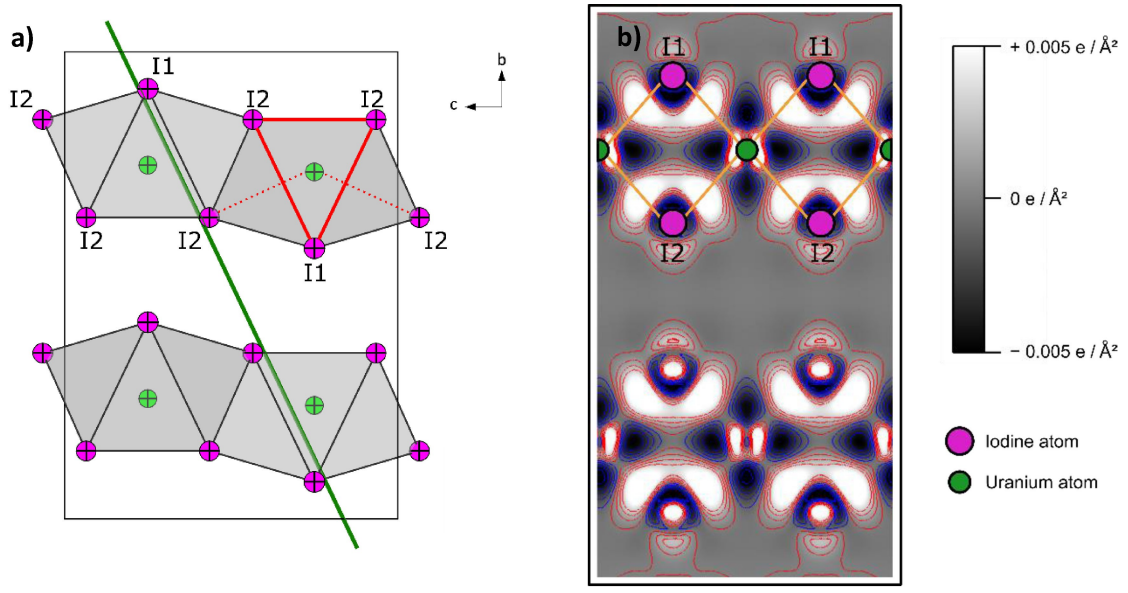

Figure 3. a) The crystal structure of UI_3 projected along [100] highlighting the layered structure and the bicapped trigonal prismatic coordination sphere of the uranium atoms. The trigonal faces are highlighted with red lines, the capping iodine atoms with dotted lines in the top right part of the figure. The iodine atoms are labeled according to the single crystal structure. The green line represents a plane parallel to the $(0\bar{2}3)$ lattice plane and including the point 0, $^1/_2$, $^1/_2$. For this plane an electron density difference map was calculated. b) Electron density difference map ($\rho_{SCF} - \rho_{atom}$) of UI_3 parallel to the $(0\bar{2}3)$ plane; density increase: white + red line, density decrease: black + blue line. The positions of the atoms and their shortest links are sketched at the top of the figure (PBE + *U*/PAW + SOC, $U = 2.60$ eV, $J = 0.45$ eV).

bonding interactions within the UI_3 layers which are themselves connected by weaker van der Waals forces.

Figure 4a and b display the band structure as well as the density of states (DOS) of UI_3 calculated with PBE and PBE + *U*, respectively. The calculations were performed with relativistic pseudopotentials including spin-orbit interactions using the experimentally determined crystal structure as input. Details are given in Section 4.4. In both calculations the iodine 5*p* states form the lower part of the valence band. The conduction band is formed by the uranium 5*f* states. In case of the PBE band structure (Figure 4a) the 5*f* band is split into three parts. One of them is filled and lies below the Fermi level that is located at a local minimum of the DOS. This band has predominantly $5f_{5/2}$ character as shown in the projected DOS on the right side of Figure 4a. This is in line with Hund's coupling rules stating that for less than half filled orbitals the total angular momentum *J* couples as *L*–*S*.

The PBE functional predicts UI_3 to be a metal with low electrical conductivity: Two bands are crossing the Fermi level. However, it is a well-known issue of GGA functionals to underestimate band gaps due to self-interaction errors.[16] It is thus likely that onside Coulomb interactions of the uranium 5*f* electrons are underestimated by this approach as discussed above. To account for this effect, we also have applied the GGA + *U* approach on the calculation of the electronic structure. The resulting band structure is shown in Figure 4b. The included onside Coulomb and exchange interactions push the uranium 5*f* bands marked by an arrow in Figure 4a apart and thus a small band gap opens of about 1 eV. The size of the band gap lies in the infrared absorption region and is thus in line with the black color of UI_3.

The band structures shown in Figure 4 are given along two high-symmetry lines. The first path on the left side includes the band dispersion predominantly in the *ac* plane. The second path on the right side displays the dispersion predominantly along the *b* axis. The comparison of these two paths thus yields information about the two-dimensional anisotropy induced by the layered structure of UI_3 into the electronic structure of this compound. The differences are most noticeably in the uranium *f* bands. As shown in Figure 4a, these bands are almost flat along the A–A_1–X_1–X path and do not cross each other. This is in line with the insignificant overlap of the uranium *f* bands along the *b* axis and between the UI_3 layers. In contrast, the uranium *f* bands display a remarkable dispersion parallel to the *ac* plane. This is even more pronounced in case of the PBE + *U* calculations shown in Figure 4b. The unoccupied uranium bands between 1 and 3 eV have an overall dispersion of 2 eV within the *ac* plane, whereas the dispersion along the A–A_1–X_1–X path is only approximately 1 eV.

The anisotropy of the electronic band structure dispersion is therefore in line with our discussions concerning the electron density. Both investigations hint towards strong bonding interactions within the UI_3 layers. The layers themselves are connected by van-der Waals forces as demonstrated by our structural calculations with and without dispersion interactions.

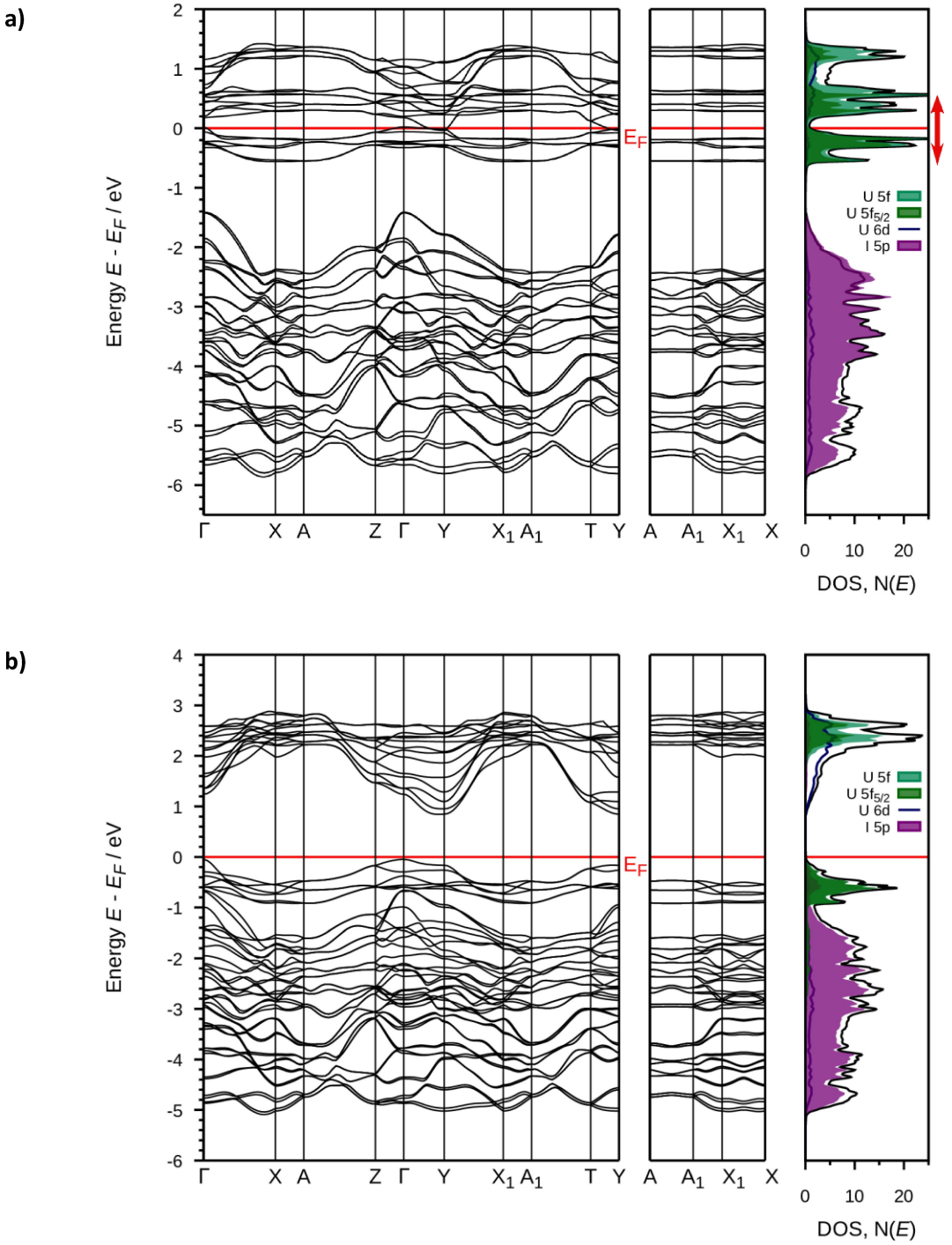

Figure 4. Band structure along high-symmetry lines and DOS of UI_3. a) PBE/PAW + SOC. The arrow marks the bands that are shifted by the PBE + *U* correction. b) PBE + *U*/PAW + SOC, $U = 2.60$ eV, $J = 0.45$ eV.

3. Conclusion

We confirmed by powder neutron diffraction that UI_3 crystallizes in the $PuBr_3$ structure type, space group *Cmcm*. Neither could we detect temperature dependent phase changes by magnetic measurements, nor by measurements of the heat capacity, both in the temperature range from 1.8 to 300 K. UI_3 displays pronounced anisotropic effects due to its layered structure. We could demonstrate these effects by DFT calculations on the structural and electronic properties of UI_3. We showed that plain GGA calculations cannot capture the dispersion interactions as well as correlation effects present in UI_3. Applying semiempirical dispersion corrections as well as a Hubbard-*U* correction accounting for the correlated *f* electrons of the uranium atoms

yield satisfactory results for the calculation of the structural as well as electronic properties of UI_3.

Experimental section

Synthesis of UI_3

UI_3 was synthesized according to the literature.[4] All work was carried out excluding humidity and air in an atmosphere of dried and purified argon (5.0, Westfalen AG) using high-vacuum glass lines or a glovebox (MBraun). Silicon (Alfa Aesar −100 mesh 99.9 %) was used as supplied. All glass vessels were made of borosilicate glass and flame-dried under vacuum before use. Each ampoule was charged with 1000 mg of finely ground UI_4 (1.34 mmol, 20 mg excess) and 9.23 mg Si (0.33 mmol) and flame sealed under vacuum ($1 \cdot 10^{-3}$ mbar). The starting materials were reacted at 450 °C for 7 days before the chemical vapor transport reaction was conducted with a source temperature of 450 and a sink temperature of 300 °C. The yield is essentially quantitative with respect to silicon. The uranium triiodide was additionally analyzed by powder X-Ray diffraction and IR spectroscopy as presented in the literature.[4] The small amount of Si (< 1 wt.%) remained undetected by these methods but was observable in the powder neutron diffraction experiment. It is unclear as to why some Si starting material was left over.

Powder neutron diffraction

The powder patterns of UI_3 were recorded in a vanadium ampoule of 8 mm inner diameter and of approximately 50 mm height at temperatures of 10, 100, and 298 K using the SPODI neutron powder diffractometer ($\lambda = 1.548$ Å) at the research reactor FRM II.[17]

Rietveld Refinements[18] were performed using the TOPAS-Academic software (Version 7).[19] As a starting point for the refinements, a former structure model was used and the data of all three measurements were refined using the same initial parameters.[1] A shifted 8-term Chebyshev polynomial was used to describe the background, peak profiles were fitted using a modified Thompson-Cox-Hastings pseudo-Voigt ("TCHZ") function as implemented in TOPAS and zero shift was refined. A fourth-order spherical harmonic function was used to consider the strong preferred orientation of the crystals. The final refinement cycles converged with free refinement of all background, profile and lattice parameters, including the coordinates and isotropic displacement parameters of all atoms. We have deposited the temperature dependent crystal structure data of UI_3 at the CCDC/FIZ Karlsruhe deposition service under the deposition number 2060056, 2060057 and 2060058 for the data at 293, 100, and 10 K, respectively.

Heat capacity and magnetic measurements

Heat capacity and magnetic measurements were performed with a DynaCool system of LOT-Quantum Design. The isobaric heat capacity $C_p(T)$ was measured using the Quantum Design heat capacity option in the temperature range from 1.8 to 300 K. The UI_3 sample was crushed to a powder and compacted to small pellets ($d = 2.8$ mm) with a hydrostatic press. Graphite (Johnson Matthey GmbH, 99.999 %) was added to the samples (10 to 20 wt.%) to improve the stability of the powder pellets, as well as their thermal conductivity. As graphite undergoes no phase transitions in the investigated temperature range it does not influence the qualitative $C_p(T)$ measurements. The powder pellets were attached to the heat capacity puck of the DynaCool system using Apiezon N grease for thermal coupling to the platform.

DC-magnetic data were collected with the aid of the Quantum Design VMS option. Temperature dependent magnetic data were recorded in the range from 1.8 to 300 K with an applied field of 10 kOe. The collected data were corrected with respect to the diamagnetic moment of the polypropylene sample holder.

Quantum chemical calculations

We performed total energy calculations and structural optimizations in the framework of DFT using the software package *Quantum Espresso* version 6.6 that is based on plane-waves and pseudopotentials.[20,21] We employed the GGA-PBE exchange-correlation functional and projector augmented wave (PAW) pseudopotentials. We used scalar relativistic as well as full relativistic PAWs to account for spin-orbit coupling (SOC). In case of the iodine atoms we applied a pseudopotential from the pslibrary version 1.0.0 with no semi-core states and a $5s^2\ 5p^5$ valence configuration.[22] In case of the uranium atom, we constructed optimized PAWs using the *atomic* code distributed with the *Quantum Espresso* package. The uranium PAWs include the 6*s* and 6*p* semi-core states and two projectors per angular momentum channel. The detailed setup for the generation of the uranium PAWs as well as benchmark results are given elsewhere.[23] All calculations were performed using a 55 Ry kinetic-energy and a 440 Ry charge-density cutoff, a Marzari-Vanderbilt cold smearing of 0.02 Ry and a centered 6×6×5 k-points grid.

Structural optimizations were conducted using scalar relativistic pseudopotentials with experimental data[3] at 4.5 K as starting point. We used three different levels of theory: plain PBE,[24] PBE together with the semiempirical D3 dispersion correction of Grimme[11] and coworkers and Becke-Johnson damping labeled as PBE + D3, as well as PBE + D3 + *U* to account for the onside Coulomb interactions of the uranium 5*f* electrons. We used the simplified DFT + *U* scheme of Cococcioni and Gironcoli[25] with the fully localized limit (FFL) double counting correction as implemented in the *Quantum Espresso* package. The effective Coulomb interaction *U* of 2.6 eV was calculated by Density-Functional-Perturbation Theory (DFPT) as implemented in the code hp.x of the *Quantum Espresso* package at the experimentally determined crystal structure at 4.5 K using a 2×2×2 *q*-points grid.[15]

The electronic structure was calculated using the experimentally determined structural data at 4.5 K. We used full relativistic PAWs to account for spin-orbit coupling (SOC). We performed GGA as well as GGA + *U* calculations using the rotationally invariant scheme of Liechtenstein and coworkers with the fully localized limit (FFL) double counting correction.[26] We applied the effective Coulomb interaction from our DFPT results and an effective exchange interaction *J* of 0.4 eV taken from the literature.[27] Compared to the experimentally determined antiferromagnetic structure forming a 2×2×2 supercell,[3] we simplified the magnetic structure to a ferromagnetic interaction in the paramagnetic unit cell. The magnetic moments were oriented along the *a* axis as determined experimentally.

Acknowledgement

Extensive calculations on the MaRC2 high-performance computer of the Philipps-University Marburg were conducted for this research. The authors would like to thank the Hessian Competence Center for High Performance Computing – funded

by the Hessen State Ministry of Higher Education, Research and the Arts – for helpful advice. The quantum chemical calculations of this work were performed with the Open-Source code Quantum Espresso. The authors would like to thank the Quantum Espresso community to maintain and provide this code for publicity. The authors would also like to thank Dr. Frank Tambornino and Dr. Sergei Ivlev for advice and expertise in using the TOPAS Software. Open access funding enabled and organized by Projekt DEAL.

[1] W. H. Zachariasen, *Acta Crystallogr.* **1948**, *1*, 265–268.
[2] J. H. Levy, J. C. Taylor, P. W. Wilson, *Acta Crystallogr. Sect. B* **1975**, 880–882.
[3] A. Murasik, P. Fischer, W. Szczepaniak, *J. Phys. C* **1981**, *14*, 1847.
[4] S. S. Rudel, H. L. Deubner, B. Scheibe, M. Conrad, F. Kraus, *Z. Anorg. Allg. Chem.* **2018**, *644*, 323–329.
[5] L. D. Roberts, R. B. Murray, *Phys. Rev.* **1955**, *100*, 650–654.
[6] E. R. Jones, M. E. Hendricks, J. A. Stone, D. G. Karraker, *J. Chem. Phys.* **1974**, *60*, 2088–2094.
[7] J. A. Wilson, A. D. Yoffe, *Adv. Mater.* **1969**, *18*, 193–335.
[8] M. S. Dresselhaus, G. Dresselhaus, *Adv. Phys.* **1981**, *30*, 139–326.
[9] B. Pałosz, *Phys. Status Solidi A* **1983**, *77*, 11–34.
[10] M. Renninger, *Z. Phys.* **1937**, *106*, 141–176.
[11] S. Grimme, J. Antony, S. Ehrlich, H. Krieg, *J. Chem. Phys.* **2010**, *132*, 154104.
[12] S. Grimme, S. Ehrlich, L. Goerigk, *J. Comput. Chem.* **2011**, *32*, 1456–1465.
[13] B. Himmetoglu, A. Floris, S. de Gironcoli, M. Cococcioni, *Int. J. Quantum Chem.* **2014**, *114*, 14–49.
[14] H. J. Kulik, *J. Chem. Phys.* **2015**, *142*, 240901.
[15] I. Timrov, N. Marzari, M. Cococcioni, *Phys. Rev. B* **2018**, *98*, 085127.
[16] P. J. Hasnip, K. Refson, M. I. J. Probert, J. R. Yates, S. J. Clark, C. J. Pickard, *Philos. Trans. R. Soc. London Ser. A* **2014**, *372*, 20130270.
[17] M. Hoelzel, A. Senyshyn, N. Juenke, H. Boysen, W. Schmahl, H. Fuess, *Nucl. Instrum. Methods Phys. Res. Sect. A* **2012**, *667*, 32–37.
[18] H. M. Rietveld, *J. Appl. Crystallogr.* **1969**, *2*, 65–71.
[19] A. A. Coelho, *J. Appl. Crystallogr.* **2018**, *51*, 210–218.
[20] P. Giannozzi, et al., *J. Phys. Condens. Matter* **2009**, *21*, 1–19.
[21] P. Giannozzi, O. Andreussi, T. Brumme, O. Bunau, M. Buongiorno Nardelli, M. Calandra, R. Car, C. Cavazzoni, D. Ceresoli, M. Cococcioni, N. Colonna, I. Carnimeo, A. Dal Corso, S. de Gironcoli, P. Delugas, R. A. DiStasio, A. Ferretti, A. Floris, G. Fratesi, G. Fugallo, R. Gebauer, U. Gerstmann, F. Giustino, T. Gorni, J. Jia, M. Kawamura, H.-Y. Ko, A. Kokalj, E. Küçükbenli, M. Lazzeri, M. Marsili, N. Marzari, F. Mauri, N. L. Nguyen, H.-V. Nguyen, A. Otero-de-la-Roza, L. Paulatto, S. Poncé, D. Rocca, R. Sabatini, B. Santra, M. Schlipf, A. P. Seitsonen, A. Smogunov, I. Timrov, T. Thonhauser, P. Umari, N. Vast, X. Wu, S. Baroni, *J. Phys. Condens. Matter* **2017**, *29*, 465901.
[22] A. Dal Corso, *Comp. Mater. Sci.* **2014**, *95*, 337–350.
[23] M. Sachs, A. J. Karttunen, F. Kraus, *J. Phys. Condens. Matter* **2019**, *31*, 025501.
[24] J. P. Perdew, K. Burke, M. Ernzerhof, *Phys. Rev. Lett.* **1996**, *77*, 3865–3868.
[25] M. Cococcioni, S. de Gironcoli, *Phys. Rev. B* **2005**, *71*, 035105.
[26] A. I. Liechtenstein, V. I. Anisimov, J. Zaanen, *Phys. Rev. B* **1995**, *52*, R5467–R5470.
[27] B. Amadon, *Phys. Rev. B* **2016**, *94*, 115148.

Manuscript received: February 8, 2021
Revised manuscript received: April 12, 2021
Accepted manuscript online: April 16, 2021

